Physics of Fluids

Simulated stress mitigation strategies in embedded bioprinting

Cite as: Phys. Fluids **34**, 083112 (2022); https://doi.org/10.1063/5.0102573
Submitted: 10 June 2022 • Accepted: 04 August 2022 • Accepted Manuscript Online: 06 August 2022 • Published Online: 30 August 2022

Leanne M. Friedrich, Ross T. Gunther and Jonathan E. Seppala

Simulated stress mitigation strategies in embedded bioprinting

Cite as: Phys. Fluids **34**, 083112 (2022); doi: 10.1063/5.0102573
Submitted: 10 June 2022 · Accepted: 4 August 2022 ·
Published Online: 30 August 2022

View Online Export Citation CrossMark

Leanne M. Friedrich,[1,a)] Ross T. Gunther,[2] and Jonathan E. Seppala[1]

AFFILIATIONS

[1]National Institute of Standards and Technology, 100 Bureau Drive, Gaithersburg, Maryland 20899, USA
[2]Georgia Institute of Technology, North Ave. NW, Atlanta, Georgia 30332, USA

Note: This paper is part of the special topic, Advanced Rheology of Complex Fluids for Next-Generation Technologies.
[a)]**Author to whom correspondence should be addressed:** Leanne.Friedrich@nist.gov

ABSTRACT

Extrusion-based bioprinting is a powerful tool for fabricating complex cell-laden constructs. Embedded ink writing (EIW) is an extrusion-based printing technique wherein a nozzle embedded into a support bath writes continuous filaments. Because it allows for low-viscosity inks, EIW is particularly useful for bioprinting. One of the largest challenges in extrusion-based bioprinting is limiting the damage that cells experience inside the nozzle. Longer shear stress durations and higher shear stress magnitudes lead to more damage. Shape fidelity is also critical for bioprinting. Filaments in EIW can exhibit defects such as sharp edges and large aspect ratios, which can lead to porosity, surface roughness, and poor mechanical properties in the final part. We use numerical computational fluid dynamics simulations in OpenFOAM to evaluate whether common shear stress mitigation techniques improve cell viability without causing shape defects. Critically, we find that using a conical nozzle, increasing the nozzle diameter, decreasing the print speed, and decreasing the ink viscosity can improve the viability of stress magnitude-sensitive cells, but using a conical nozzle, increasing the nozzle length, and decreasing the print speed can increase damage in stress duration-sensitive cells. Additionally, using a conical nozzle or a larger nozzle can lead to larger shape defects in printed filaments. Material selection and printing parameter selection in embedded bioprinting should take into account allowable shape defects, allowable cell damage, and cell type.

Published by AIP Publishing. https://doi.org/10.1063/5.0102573

I. INTRODUCTION

In recent years, three-dimensional (3D) printing has revolutionized manufacturing to enable intricate, individually customizable designs. In particular, bioprinting has expanded the possibilities for tailored therapeutic devices and enhanced the allowable geometric complexity of cell scaffolds and cell-containing constructs. Direct ink writing (DIW), wherein a fluid ink is extruded as a continuous filament out of a nozzle and then solidified on a substrate, has demonstrated good suitability for bioprinting because it can employ materials with a wide variety of properties and curing methods.[1] However, DIW requires self-supporting inks which behave as viscous fluids during extrusion and elastic solids after deposition. Embedded ink writing (EIW), also known as embedded 3D printing, freeform reversible embedding, and other aliases, allows for inks which are not self-supporting.[2] In EIW, the nozzle is embedded into a viscoelastic support bath and writes continuous filaments. The bath behaves elastically and holds the form of the printed structure under static conditions, but the nozzle yields the bath during travel, allowing the bath to flow around the nozzle. Because the support fluid is responsible for form holding, EIW allows for inks that have lower viscosities and limited elastic behavior. As such, EIW is particularly useful for bioprinting of soft bioactive inks.[3] Additionally, the support fluid can contain nutrients which support cell growth after printing.[4]

The greatest challenge of printing cell-laden inks is ensuring that cells survive the printing process and proliferate afterward. Damage could entail the rupture of the cell membrane, mechanical damage to the cytoskeleton, change in or loss of function due to mechanical signaling, or an inability to proliferate after printing.[5–7] The main strategy for improving cell survival during printing is to limit the magnitude and duration of shear stresses within the nozzle.[5,8–11] Several models have been proposed that relate the fraction of damaged cells D to shear stress τ and duration t. At the simplest, D scales with $a\tau^b t^c$, where a, b, and c are cell-specific constants.[8,10] To impose bounds on the survival fraction, between 0 and 1, Ning *et al.* propose that the survival fraction $S = 1 - D$ can take an exponential form,[11]

$$S = \exp\left(-a\tau^b t^c\right). \quad (1)$$

By imposing an exponential form on the model, Ning *et al.* are able to maintain the positive correlation between shear stress and damage and the positive correlation between exposure time and damage while improving the fit of the regression for Schwann cells and myoblasts and imposing physically possible bounds on the survival fraction.[11] These models are plotted in Figs. S1 and S2. More complex models which precisely fit experimental data have been proposed.[5,8] Across all models, the common theme is that longer times in the nozzle and higher shear stresses cause more damage. In this work, we use Eq. (1) to estimate cell survival within these simulated nozzles. We use three sets of parameters. First, ($a = 1$, $b = 0$, $c = 1$) reflects cell survival functions that only depend on the duration of stress. Second, ($a = 10^{-2}$, $b = 0.5$, $c = 0.5$) is similar to the scaling determined in Ref. 11 for Schwann cells and myoblasts in alginate, where survival depends on both stress magnitude and duration. Third, ($a = 10^{-3}$ or $a = 10^{-4}$, $b = 1$, $c = 0$) reflects cell survival functions which only depend on the magnitude of stress. a values were chosen to scale all three models to a similar range, but they overestimate cell damage compared to the a values fitted in Ref. 11. The purpose of this set of models is to probe the extremes of how survival can scale with stress and duration. While the second model reflects how a cell–matrix combination similar to myoblasts in alginate will respond to the probed printing parameters, the first can be used to predict how the survival scaling will change for a cell–matrix combination that depends much more strongly on duration, and the third can be used to predict how the survival scaling will change for a cell–matrix combination that depends much more strongly on the magnitude of stress. While a value of ($b = 1$, $c = 0$) or ($b = 0$, $c = 1$) is unlikely, these models allow us to probe the underlying physics of the printing process, rather than calibrating a specific cell line in a specific matrix.

Several strategies have been proposed to limit shear stresses within the nozzle. A larger nozzle diameter, slower extrusion speed, or lower viscosity ink can decrease the shear stress.[3,5,6,9,12–16] Alternatively, a conical or tapered nozzle can lower the average shear stress by lowering the ink velocity and keeping cells away from the nozzle walls.[9] However, these treatments can also increase the duration of time that cells spend inside the nozzle, potentially harming cell survival. These stress-mitigating strategies can also impact printing performance. Filament cross sections in embedded ink writing tend to be tall and narrow and, particularly at zero surface tension, can exhibit sharp top edges.[17–24] Oblong cross sections can produce anisotropy by lowering the out-of-plane resolution and raising the in-plane resolution and can complicate toolpath design for printing freeform, three-dimensional paths. Sharp edges can introduce internal porosity and external roughness to the printed part. This work identifies tradeoffs between cell survival and morphological filament defects in embedded ink writing.

In this work, we use computational fluid dynamics simulations to predict the effect of common stress mitigation strategies on the shape of extruded filaments in embedded ink writing. While analytical solutions exist for velocities and stresses inside the nozzle for Newtonian fluids (see the supplementary material), there is no analytical solution for the shape of the extruded filament, and numerical solutions are necessary for Herschel–Bulkley fluids. Numerical simulations allow us to simultaneously inspect survival metrics and shape fidelity metrics. Simulations also enable high resolution measurements of viscosity, velocity, and shear stress inside the three-dimensional nozzles, which can be difficult or expensive to achieve in experiments. Finally, simulations allow us to isolate physical effects which would be difficult to isolate in real life. First, we can precisely control the geometry of the nozzle, whether tapered or cylindrical. We can make the ink and support identical in rheology and density, avoiding the changes that can occur when dyes are introduced for visual contrast.[24] Moreover, we can isolate individual elements of the rheology. To isolate viscous dissipation from yielding effects, we simulate both Newtonian fluids and Herschel–Bulkley fluids.

In EIW, the support bath is usually a viscoelastic fluid. Previous works have used granular gels composed of poly(acrylic acid) particles or Carbopol, in water,[25] nanoparticulate suspensions such as Laponite in water,[26] chopped slurries such as gelatin,[27] and organoid suspensions.[28] Though EIW enables lower viscosities and lower yield stresses than DIW, most EIW inks are also viscoelastic. Yield stress fluid inks used in bioprinting include gelatin methacrylate,[19] Pluronic F127,[29] and bio-inks with additives including methylcellulose, xanthan gum, gelatin microparticles, and Laponite nanoparticles.[28] Most of these viscoelastic fluids follow the Herschel–Bulkley model, which describes solid-like behavior below a yield stress and shear thinning fluid-like behavior above yield. In addition to Herschel–Bulkley parameters fit to experimental measurements for Carbopol,[30] we vary the shear-thinning behavior of the Herschel–Bulkley fluids using the consistency index k.

Some works have demonstrated printing of Newtonian inks into Newtonian supports. Typically, these are low-viscosity, immiscible inks, and supports with particle-stabilized interfaces.[31,32] Some inks and supports are viscous, do not have a yield stress, and have minimal shear thinning, such as certain alginate compositions.[17] Additionally, many types of culture media are Newtonian.[33] To isolate the effect of local viscous dissipation from the effects of yielding and shear thinning, we simulate Newtonian inks printed into Newtonian supports, where the viscosity is the local viscosity of the ink and support near the nozzle for the Herschel–Bulkley fluids in this work. Furthermore, to probe the scaling of survival and defects with viscous dissipation, we simulate Newtonian fluids across a range of viscosities.

Previously, we found that OpenFOAM simulations like the ones in this work accurately predict trends in the aspect ratio, but they underestimate filament aspect ratios compared to experiments.[24] As such, within this paper, shorter aspect ratios and smoother surfaces are ideal, even when they appear to be vertically compressed.

II. NUMERICAL MODEL

Simulations were performed in OpenFOAM 8,[34] using similar methods to Ref. 20.[35] OpenFOAM is an open source volume of a fluid numerical computational fluid dynamics solver. Input files and analysis code were written in Python 3.8[36] using code available at Ref. 37. Analysis also employed Paraview 5.10.0.[38] The data associated with this paper are available at Ref. 39. For 2.5 s of simulated flow, without parallelization of individual simulations, on a high performance computing cluster, each of the 65 simulations ran for 2–371 h in real time. Note that these fluids do not reach steady state, and the shape of the interface continually evolves.[20] However, residuals do converge within 2.5 s (Fig. S7). As such, values are collected at 2.5 s for all simulations, instead of seeking an unreachable steady state.

A. Geometry

The mesh was created with snappyHexMesh, which establishes a prismatic mesh that is refined at the internal and external surfaces of the nozzle.[34] SnappyHexMesh used up to four levels of snapping mesh refinement at the nozzle walls and two levels of snapping mesh refinement at the nozzle inlet (a finer mesh than Ref. 20). The maximum number of cells was set to 20×10^6 cells, but most simulations ranged between 1.5×10^6 and 3×10^6 cells. For nozzle inner diameters d_i smaller than 0.8 mm, the initial cell size was 0.2 mm. For the larger nozzle, the initial cell size was $0.2/0.603 \times d_i$ mm. Inscrutably, using a finer, proportional initial cell size for the small nozzles led to unfeasibly large solve times, so the coarser mesh is reported here, with obvious mesh artifacts. Dynamic remeshing was imposed at the ink–support interface, down to four levels of a finer mesh and up to five levels of a coarser mesh. Variations in filament shape between four levels of refinement and five levels of refinement are small (Fig. S8).

The simulated geometry and boundary conditions are shown in Fig. 1. A nozzle of angle θ, outlet inner diameter d_i, and wall thickness t_w the nozzle remains static. The thickness t_w is defined in the x–y plane, not necessarily normal to the nozzle walls. The inner, outer, and bottom walls of the nozzle, which have a fixedWalls boundary condition, have a no slip velocity condition and a zero gradient composition and pressure condition. The upstream, bottom, and left and right faces of the bath have a bathFlow condition, wherein the composition is all support material, the velocity is fixed at the print speed, and there is zero pressure flux over the boundary. The inkFlow boundary is imposed on the nozzle inlet. The flow of ink into the inlet of the nozzle has a fixed velocity, which is equal to the bath translation velocity multiplied by the nozzle outlet area divided by the nozzle inlet area. As such, the ink speed, or the flux of ink through the nozzle divided by the area of the nozzle outlet, is equal to the stage speed. The inkFlow boundary has zero pressure flux over the boundary, and the composition is all ink. The top and downstream faces of the bath have an atmosphere condition that mimics a plane near the bath surface, such that the total pressure is zero over the surface, but ink and support can flow in and out. The velocity condition at the atmosphere is a pressureInletOutletVelocity condition, which imposes a zero gradient condition on the velocity out of the surface and bases the velocity into the surface on the flux of fluid normal to the surface necessary for mass conservation. The internal mesh elements are initialized at a pressure of 0 and velocity of 0. Inside the nozzle, the composition is initialized as only ink, and outside the nozzle, the composition is initialized as only support. The bath is a constant $10d_i$ in y width, $16d_i$ in x length, and $7d_i$ in z height. The center of the nozzle is $4d_i$ from the upstream face of the bath. For the speed sweep at a nozzle angle of 0°, a slightly smaller bath was simulated, with a width of $7d_i$. In all cases, the center of the nozzle was $4d_i$ from the upstream face of the bath. The bottom of the nozzle was $d_i/2$ above the midpoint of the bath. For the nozzle angle sweep, a bath size which increased with nozzle angle was tested, indicating the same trend but slightly different values (Fig. S9).

Unless otherwise noted, the nozzle is a 20 gauge blunt tipped needle with an inner diameter d_i of 0.603 mm and a wall thickness t_w of 0.152 mm. Other probed nozzle dimensions are 18 gauge ($d_i = 0.838$, $t_w = 0.216$ mm), 22 gauge ($d_i = 0.413$, $t_w = 0.152$ mm), and 25 gauge ($d_i = 0.26$, $t_w = 0.127$ mm). Unless otherwise noted, the needle is cylindrical. Conical nozzles with angles of 5°, 10°, 15°, 20°, 25°, and 30° were also simulated. Unless otherwise noted, the print speed, which refers to both the average ink speed out of the nozzle outlet and the bath translation speed, is 10 mm/s. Speeds of 5, 7.5, 12.5, and 15 mm/s were also probed.

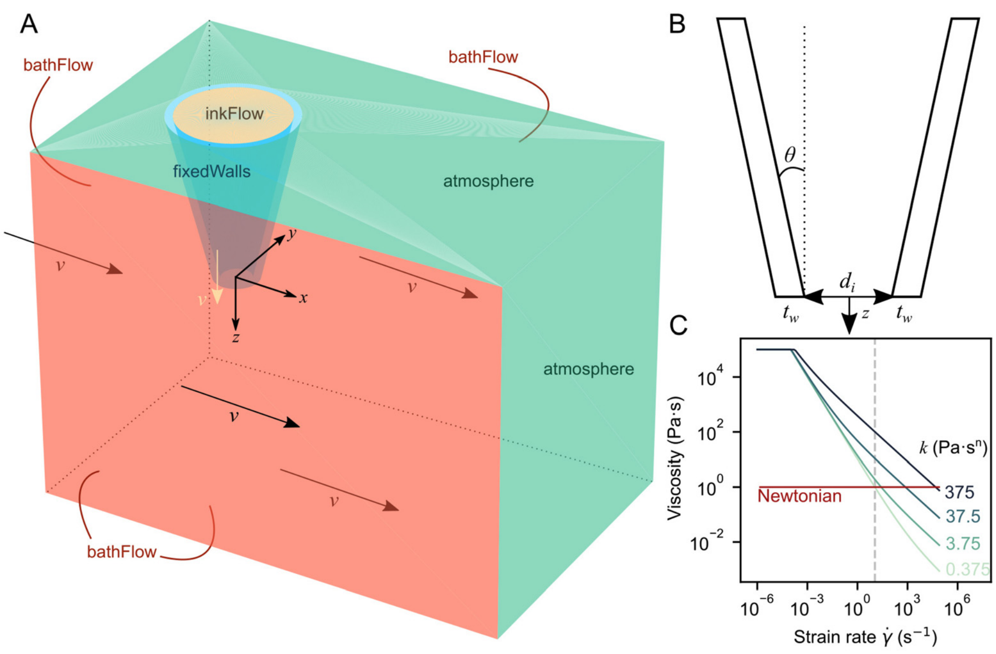

FIG. 1. (a) Boundaries of the simulation. The gray lines indicate boundaries between mesh cells. Ink flow speed and support translation speed are equal, at velocity v. (b) Nozzle angle θ, inner diameter d_i, and wall thickness t_w. (c) Viscosities of simulated Herschel–Bulkley and Newtonian fluids. The gray dashed line indicates the support shear rate $\dot{\gamma} = v/(d_i + 2t_w)$, where the print speed is 10 mm/s and the nozzle is a 20 gauge cylindrical needle.

B. Material properties

The ink and support are identical. Unless otherwise noted, the ink and support are Herschel–Bulkley fluids. In OpenFOAM, Herschel–Bulkley fluids are defined as viscous fluids below the yield stress and shear thinning fluids above the yield stress. Within the simulation, the viscosity η is defined in Eq. (2), where $\dot{\gamma}$ is the shear strain rate, η_0 is a plateau viscosity, τ_0 is the yield stress, k is the consistency index, and n is the power law index

$$\eta = \min(\eta_0, \tau_0/\dot{\gamma} + k\dot{\gamma}^{n-1}). \tag{2}$$

In this work, η_0 is 10^4 Pa s, τ_0 is 10 Pa, k is 3.75 Pa $\cdot$ s^n, and n is 0.45, which are reported values for a Carbopol in water suspension.[30] To isolate the effect of local viscosity from the effect of yielding, consistency indices of 0.375, 37.5, and 375 Pa s^n were also probed. Increasing k leads to less severe shear thinning and higher local viscosities near the nozzle [Fig. 1(c)]. To isolate the effects of viscous dissipation from the effects of yielding, Newtonian fluids of viscosity 0.1, 1, 10, 10^2, 10^3, 10^4, and 10^5 Pa $\cdot$ s were also tested, where the ink and support were identical, at varying conical nozzle angles. To suppress buoyancy, both the ink and support had a density of 1 g/ml.

While there are some examples of oil-based inks printed into water-based supports,[27] most bioprinting applications use water-based inks printed into water-based supports, which have negligible interfacial tension effects. This is most evident in experimental water-based ink and support combinations that produce filaments with sharp top edges,[21,24,40] matching the zero surface tension simulations in Ref. 20. As such, the interfacial tension σ between the ink and support was defined as 0 mN/m. The InterFoam solver treats the phase space as a continuum, where the interface is a multi-cell region containing a mixture of two immiscible, incompressible, isothermal phases, instead of defining a sharp interface.[41] Contact angles are not defined, so no contact angle correction occurs at the nozzle wall, and the no-slip condition governs the nozzle–fluid interface.

C. Governing equations

Simulations used the solver InterFoam, which is a volume of fluid solver that is described in detail in Refs. 41–43. Briefly, the space is discretized into volumetric elements which are labeled as boundary elements or internal elements. Each element is a mixture of ink and support, with volume fractions between 0 and 1, inclusive, where the Reynolds number is defined as $Re = \rho V_\infty D/\eta$, and V_∞ is the print speed, D is the nozzle diameter (inner for ink, outer for support), and η is the local viscosity at the nozzle outlet. Reynolds numbers in this work range between 6×10^{-8} and 6×10^{-2} for ink and 9×10^{-8} and 9×10^{-2} for support. At these low Reynolds numbers, we expect that turbulence is suppressed.

For each volumetric element, InterFoam solves the continuity equation [Eq. (3)], laminar flow transport equation [Eq. (4)], and mass conservation equation [Eq. (5)], where u_j is the velocity in direction j, x_j is the distance in direction j, ρ is the density, t is the time, p is the pressure, τ_{ij} is the viscous stress, g_i is the acceleration due to gravity, σ is the interfacial tension (zero here), and α_{ink} is the volume fraction of ink

$$\frac{\partial u_j}{\partial x_j} = 0, \tag{3}$$

$$\frac{\partial(\rho u_i)}{\partial t} + \frac{\partial}{\partial x_j}(\rho u_j u_i) = -\frac{\partial p}{\partial x_i} + \frac{\partial \tau_{ij}}{\partial x_j} + \rho g_i + \sigma\kappa\frac{\partial \alpha_{ink}}{\partial x_i}, \tag{4}$$

$$\frac{\partial \alpha_{ink}}{\partial t} + \frac{\partial(\alpha_{ink} u_j)}{\partial x_j} = 0. \tag{5}$$

If the interfacial tension was non-zero, the curvature κ would be approximated by Eq. (6),

$$\kappa = -\frac{\partial}{\partial x_i}\left(\frac{\partial \alpha_{ink}/\partial x_i}{|\partial \alpha_{ink}/\partial x_i|}\right). \tag{6}$$

Because the interfacial tension is assumed to be negligible, no curvature correction for interfacial tension is applied.

At boundaries between materials A and B with normal $\boldsymbol{n}$, the kinematic condition requires continuity of the normal component of the velocity [Eq. (7)]

$$\boldsymbol{u_A} \cdot \boldsymbol{n} = \boldsymbol{u_B} \cdot \boldsymbol{n}. \tag{7}$$

This condition is fulfilled by the no slip condition at the nozzle walls, the fixed velocity conditions at the inkFlow inlet of the nozzle and bathFlow faces of the bath, and the zero gradient condition on the atmosphere faces of the bath. Because the ink–support interface is not sharp in the volume of fluid method, the interface is instead governed by the mass conservation equation [Eq. (5)], where each mesh element contains a mixture of ink and support. The density of the mixture is determined using a rule of mixtures, given the ink density ρ_{ink} and support density ρ_{sup} [Eq. (8)], and the kinematic viscosity of the mixture is determined using the local kinematic ink viscosity ν_{ink} and local kinematic support viscosity ν_{sup} [Eq. (9)]. Local viscosities for Herschel–Bulkley fluids are calculated using Eq. (2)

$$\rho = \alpha_{ink}\rho_{ink} + (1 - \alpha_{ink})\rho_{sup}, \tag{8}$$

$$\nu = \alpha_{ink}\nu_{ink} + (1 - \alpha_{ink})\nu_{sup}. \tag{9}$$

The dynamic viscosity of the mixture η can, thus, be calculated using the density and kinematic viscosity

$$\eta = \rho\nu. \tag{10}$$

InterFOAM uses the PIMPLE algorithm to handle inter-equation coupling and apply boundary conditions on boundary elements.[44] Time steps are chosen with a maximum Courant number of 1.

Scalar shear stress magnitudes were computed in Paraview. First, the shear rate $\dot{\gamma}$ was determined from the velocity magnitude (via *ComputeDerivatives*[38])

$$\dot{\gamma}_i = \frac{\partial|\boldsymbol{u}|}{x_i}. \tag{11}$$

Next, the shear stress magnitude τ was determined using the dynamic viscosity and magnitude of the shear rate

$$\tau = \eta|\dot{\gamma}|. \tag{12}$$

III. RESULTS

In order to predict cell survival in these simulated nozzles, we use the model described in Eq. (1).[11] We execute the following procedure on interpolated points within the nozzle at 2.5 s of flow, which is not quite steady state for many simulations,[20] but reflects very slow changes in state. This procedure traces the approximate path that a particle takes through the nozzle, tracking the residence time and stresses experienced by the particle in order to evaluate the survival probability of a cell at the nozzle outlet. Here, radial positions within the nozzle are normalized by the inner diameter at the given longitudinal position in the nozzle, r_0. The procedure assumes that a particle at normalized radial position r/r_0 will stay at the same normalized radial position as it flows through the length of the nozzle.

We discard the top 10% of the length of the nozzle, where the velocity profile is evolving from the constant inlet velocity profile established in the boundary conditions. Slices are collected at 35 equally spaced z positions within the nozzle. At each z position along the length of the nozzle, we select only the points at $y = 0$ and at the downstream x half of the nozzle, which leads to noisier data but faster processing than averaging points [Fig. S10(a)]. The downstream half of the nozzle experiences higher stresses at the outlet (Figs. S10 and S13). These high outlet stresses come from the sharp change in fluid flow direction at the outlet. The ink experiences shearing flow at the nozzle outlet, where above the outlet, the flow has a negligible x component for cylindrical nozzles, and below the outlet, the flow has a 10 mm/s x component. At the downstream edge of a conical nozzle, this change in direction is even greater, because just above the outlet on the downstream edge, the flow has a negative x component as it follows the taper of the nozzle, and below the outlet, the flow has a positive x component. This sudden change in the direction translates into a high shear rate, which results in a high shear stress. Moreover, the sharp corners of the nozzle around which the fluid bends act as stress concentrators. This high stress region is shown in three dimensions in Fig. S13.

We group the selected points by normalized radius r/r_0, rounded to the closest 0.05 (or 0.1, for Fig. 2), where r_0 is the inner diameter at that z value, and r is the distance from the center of the nozzle. For each r/r_0, we average all points at that r/r_0 and collect the velocity magnitude v, position x, y, z, and stress magnitude τ. We calculate the time t that the fluid spends at that z step as the distance traveled since the previous z step at that r/r_0, divided by the velocity magnitude. Given values of a, b, and c, the survival fraction at that step is calculated using Eq. (1). The cumulative survival fraction is then multiplied by the survival fraction at that step.

An example of the survival calculation is shown in Fig. 2 for cells which are equally sensitive to stress magnitude and duration. For a cylindrical nozzle, the velocity and stress remain somewhat flat along

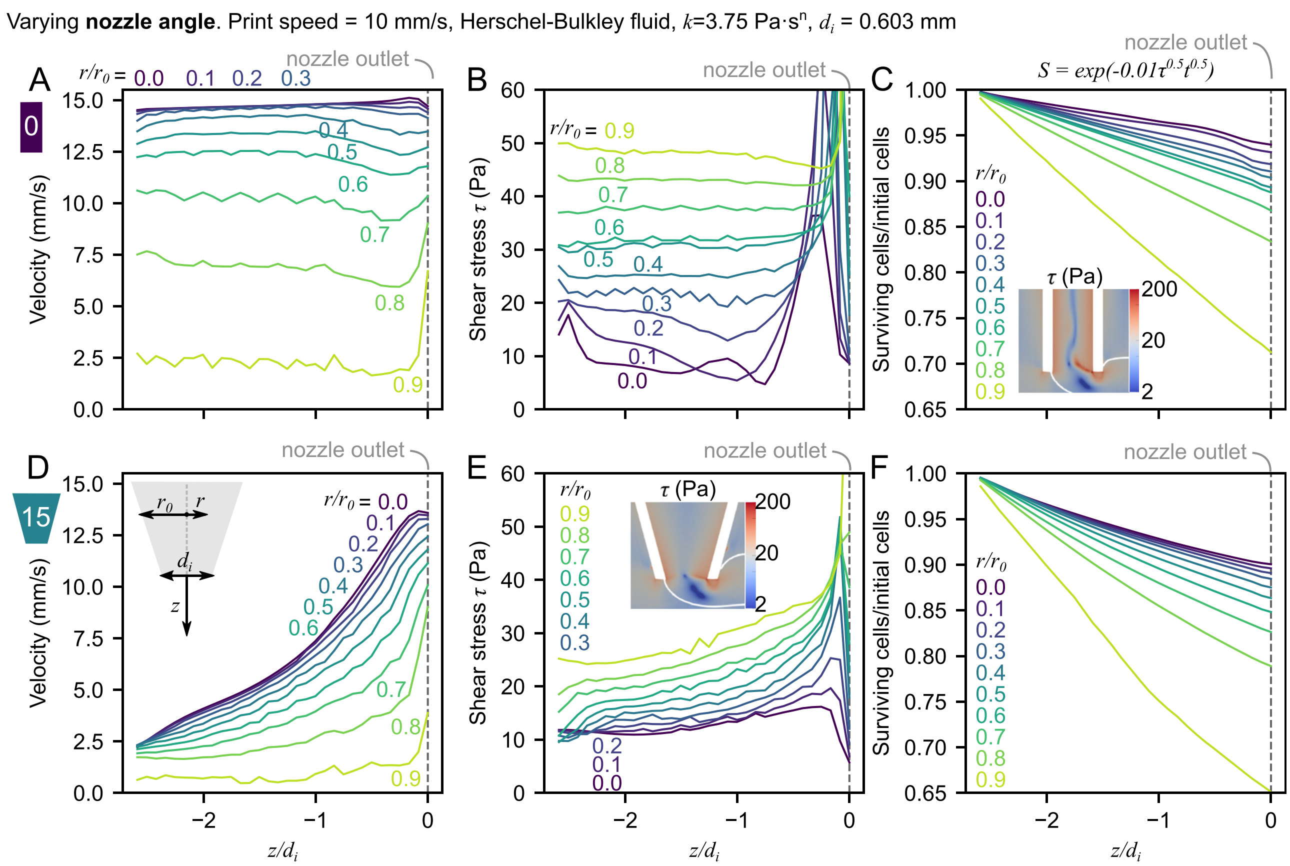

FIG. 2. Estimation of cell survival within (a)–(c) a cylindrical (0°) nozzle and (d)–(f) a conical (15°) nozzle, for a Herschel–Bulkley ink and support, with speed 10 mm/s, with a d_i of 0.603 mm after 2.5 s of flow. At each radius within the nozzle, relative to the total inner radius of the nozzle at a given z, as a function of vertical z position within the nozzle, (a) and (d) the local velocity magnitude, (b) and (e) the local shear stress magnitude, and (c) and (f) the cumulative cell survival are shown. The cumulative cell survival function assumes that survival equally depends on the magnitude and duration of the shear stress. Insets: Shear stress magnitude maps inside (c) cylindrical nozzle and (e) conical nozzle.

the length of the nozzle [Figs. 2(a) and 2(b)]. The stress spikes at the outlet, peaking at the downstream corner of the nozzle [Figs. 2(c) inset and S13]. The fluid is slowest and experiences the highest stresses near the nozzle walls ($r/r_0 = 0.9$). As such, the cells experience the most damage at the nozzle walls [Figs. 2(c) and 2(f)]. In cylindrical nozzles, local fluctuations in stress occur at small normalized radii because the flow of support past the outlet leads to asymmetry in the stress field near the nozzle outlet [Figs. 2(c) inset and S10(b)]. In a conical nozzle, the fluid at the edge still experiences the longest duration, highest stress, and lowest survival [Figs. 2(d)–2(f)]. However, the fluid increases in speed and shear stress as it approaches the nozzle outlet [Figs. 2(d) and 2(e)], where the scaling of magnitude and duration are equal, the slower velocities near the inlet lead to more damage at the inlet in conical nozzles than in cylindrical nozzles [Figs. 2(c) and 2(f)]. As a final step, we can estimate survival for the entire nozzle by calculating the average survival at the outlet across all radial positions, weighted by ring area.

Where the ink and support are identical Herschel–Bulkley fluids, increasing the nozzle angle changes the filament shape and can help or harm cell survival. For a cylindrical nozzle, the average shear stress across the area of the nozzle remains constant along the length of the nozzle, eventually spiking at the nozzle exit [Fig. 3(a)]. For a conical nozzle, the average shear stress across the area of the nozzle increases gradually along the length of the nozzle and spikes to a lower value than the cylindrical nozzle at the nozzle outlet [Fig. 3(a)]. This change in shear stress is due to a change in cross-sectional area across the length of the nozzle. A line trace across the nozzle $2d_i$ before the nozzle outlet indicates that the shear stress at the wall decreases as the nozzle angle increases [Fig. 3(b)]. All of the conical nozzles reach the same shear stress at the nozzle center, but the cylindrical nozzle reaches a slightly lower shear stress at the center [Fig. 3(b)]. While higher nozzle angles produce lower shear stresses, they also produce longer extrusion durations. $2d_i$ before the nozzle outlet, cylindrical nozzles exhibit plug flow (a constant velocity across the nozzle width) at the center of the nozzle and a steep decrease in speed toward the wall [Fig. 3(c)]. Conical nozzles shift to more parabolic flow with increasing nozzle angle, with lower peak velocities at the nozzle center [Fig. 3(c)].

Depending on the damage model, increasing the nozzle angle can improve or worsen cell survival. Recall that the damage models use arbitrary scaling constants a, so only trends should be compared between models, not survival values. Where cell survival depends only on duration, in cylindrical nozzles, the cell survival plateaus across the nozzle radius, then steeply decreases [Fig. 3(d)]. Increasing the nozzle angle decreases survival rates across the entire nozzle, steepening the decrease in survival toward the nozzle edge. Thus, the overall survival rate is lower for higher nozzle angles [Fig. 3(d)]. Where the survival scales equally with duration and magnitude, survival gradually decreases toward the edge, then steeply drops [Fig. 3(e)]. Increasing the nozzle angle uniformly decreases cell survival, leading to an overall decrease in survival with increasing nozzle angle [Fig. 3(e)]. Where the survival only depends on the shear stress magnitude, survival rates are the same for all nozzle angles at the center of the nozzle, but survival rates gradually decrease toward the wall [Fig. 3(f)]. Small angle nozzles experience a steeper decrease in survival toward the wall, so the survival rate increases with increasing nozzle angle [Fig. 3(f)].

Increasing the nozzle angle leads to taller, narrower filaments with a sharper top edge [Fig. 3(g)]. As the intended placement of the filament centroid is one nozzle radius below the tip of the nozzle, increasing the nozzle angle also shifts the filament centroid upward in the bath [Fig. 3(g)]. Sharper filament edges can lead to porosity or surface roughness, so larger nozzle angles may lead to more structural defects. Because we expect that these simulations underestimate filament height/width, ideal cross sections are achieved at lower nozzle angles.

Where the ink and support are identical Newtonian fluids, the same nozzle angle dependencies found for Herschel–Bulkley fluids apply. In agreement with the analytical solution (Fig. S4), in cylindrical nozzles, the shear stress remains constant throughout the nozzle and does not spike at the nozzle exit [Fig. 4(a)]. In conical nozzles, the stress plateaus at the nozzle inlet, then steeply increases at the nozzle exit. Both the plateau stress and the outlet stress decrease with increasing nozzle angle. Taking a line trace across nozzle, $2d_i$ before the outlet, the shear stress at the center of the nozzle is the same for all nozzle angles [Fig. 4(b)]. The stress increases linearly from the center to the nozzle walls, but the increase is smaller for larger nozzle angles. However, while larger conical nozzle angles exhibit lower stresses, they also experience longer durations. In Newtonian fluids, the velocity field is parabolic for all nozzle angles, and the velocity at the center increases with decreasing nozzle angle [Fig. 4(c)].

Depending on the survival function, increasing the nozzle angle for Newtonian fluids can worsen or improve cell survival. Like the trend in Herschel–Bulkley fluids, when cell survival only depends on duration, survival rates decrease more steeply toward the nozzle walls, and increasing the nozzle angle decreases survival rates across the entire nozzle [Fig. 4(d)]. If the cell survival depends equally on the shear stress magnitude and duration, survival rates are higher in the center of the nozzle but lower at the walls for conical nozzles, leading to an overall increase in survival with increasing nozzle angle [Fig. 4(e)]. Where survival only depends on stress magnitude, survival rates improve with increasing nozzle angle, largely due to improvement in survival at the walls [Fig. 4(f)].

As shown in Ref. 20, simulated Newtonian fluids exhibit taller, sharper filament cross sections than Herschel–Bulkley fluids. As the nozzle angle increases, the filaments become taller, narrower, and sharper, and they shift farther upwards in the bath downstream of the nozzle. Ridges along the side of the filament also appear with increasing nozzle angle [Figs. 4(g) and S15]. These trends confirm that the survival trends and the morphology trends exhibited in Herschel–Bulkley fluids do not just come from shear thinning, because they are still present when the viscosities of the ink and bath are constant.

The shape of the flow field provides useful context for the effect of nozzle angle on the cross-sectional shape of the filament. When the nozzle travels through the support, it displaces fluid. Fluid that is near the bottom of the nozzle is displaced below and around the sides of the nozzle. Fluid that is higher up in the bath is displaced around the nozzle, then converges behind the nozzle. The support flowing below the nozzle causes a pressure differential between the high-pressure nozzle outlet and the low-pressure downstream face of the nozzle, creating an upward flow zone directly downstream of the nozzle. The converging support pinches the filament, causing it to become tall and narrow, with a sharp top edge.[20]

Changing the nozzle angle changes the shape and direction of the flow field and alters the velocity within each of the critical flow zones.

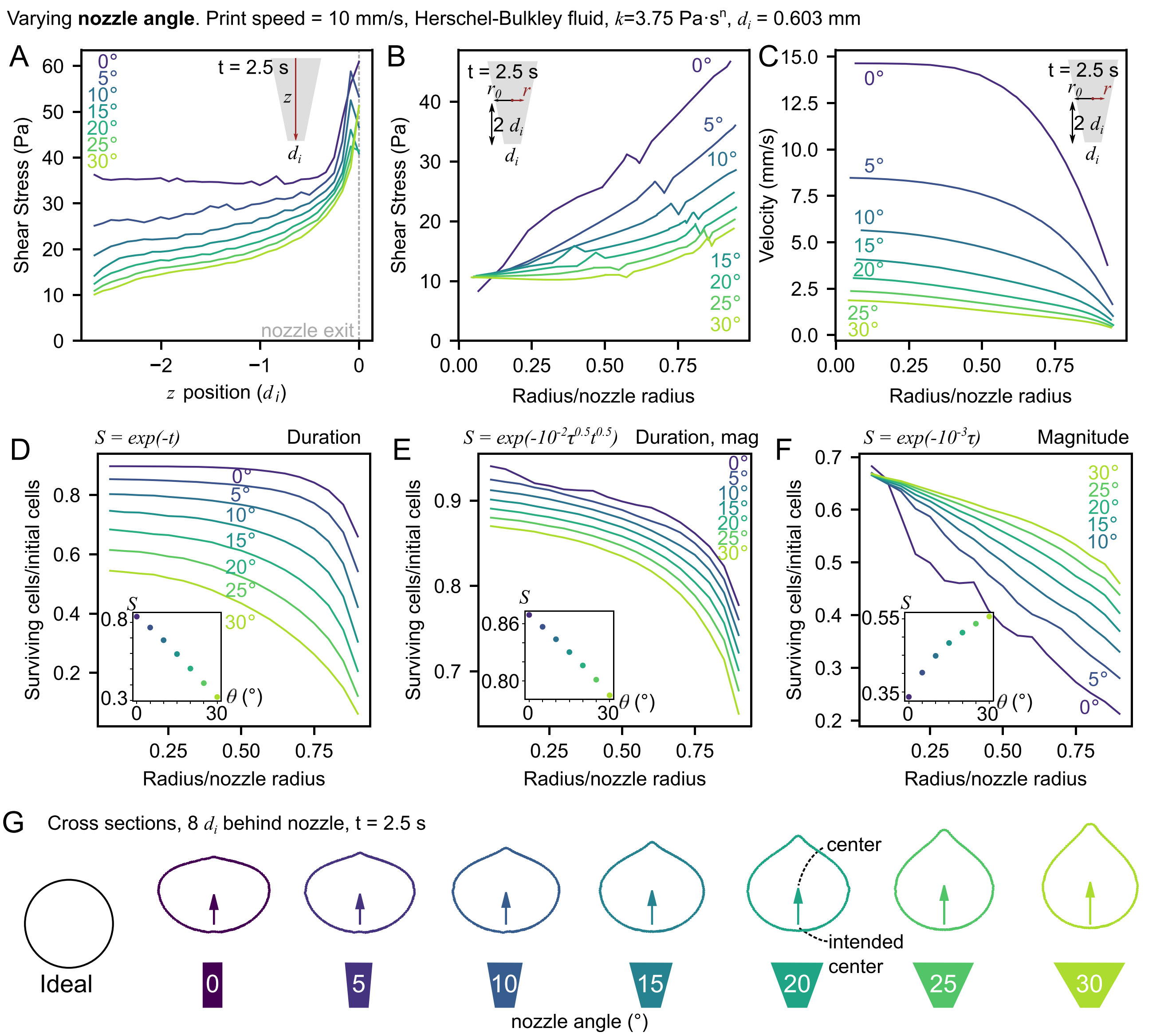

FIG. 3. The effect of nozzle angle on stresses and morphologies in Herschel–Bulkley fluids, with $k = 3.75\,\mathrm{Pa} \cdot \mathrm{s}^n$, at a print speed of 10 mm/s, after 2.5 s of flow. (a) Average shear stress across the nozzle-cross section as a function of z position along the length of the nozzle. (b) and (c) Line traces $2d_i$ above the nozzle exit across the diameter of the nozzle. (b) Shear stress as a function of radial position. (c) Velocity magnitude as a function of radial position. (d)–(f) Fraction of surviving cells as a function of radial position, for varying nozzle angles, given three different models. Inset indicates survival for all cells in the nozzle, as a function of nozzle angle. (d) Survival depends only on duration of stress. (e) Survival depends equally on magnitude and duration. (f) Survival only depends on magnitude of stress. (g) Cross-sections of extruded filaments $8d_i$ behind the nozzle. Arrows indicate the displacement between the intended center and calculated centroid of the cross section.

In both Herschel–Bulkley and Newtonian fluids, with increasing nozzle angle the fluid within and near the filament is pushed to stronger positive z velocities in the upward flow zone [Figs. 5(a) and 5(d)]. Similarly, the filament and fluid above the filament have slower x velocities, spending more time in the upward flow zone with increasing nozzle angle [Figs. 5(b) and 5(e)]. These changes in the flow field cannot merely be attributed to changes in viscosity in Herschel–Bulkley fluids because they also occur in Newtonian fluids, where the viscosity is constant [Figs. 5(c) and 5(f)].

Volume displacement provides some context for the change in the flow field with nozzle angle. In Herschel–Bulkley fluids with cylindrical nozzles, the displaced support fluid travels upward along the sides of the nozzle, then flows downward behind the nozzle as the downstream volume becomes available, producing negative z velocities which compress the filament vertically [Fig. 5(g)]. As the nozzle angle increases, more volume is displaced at higher positions on the nozzle, leading to less upward displacement of fluid around the sides of the nozzle, which are matched by smaller downward flows downstream of

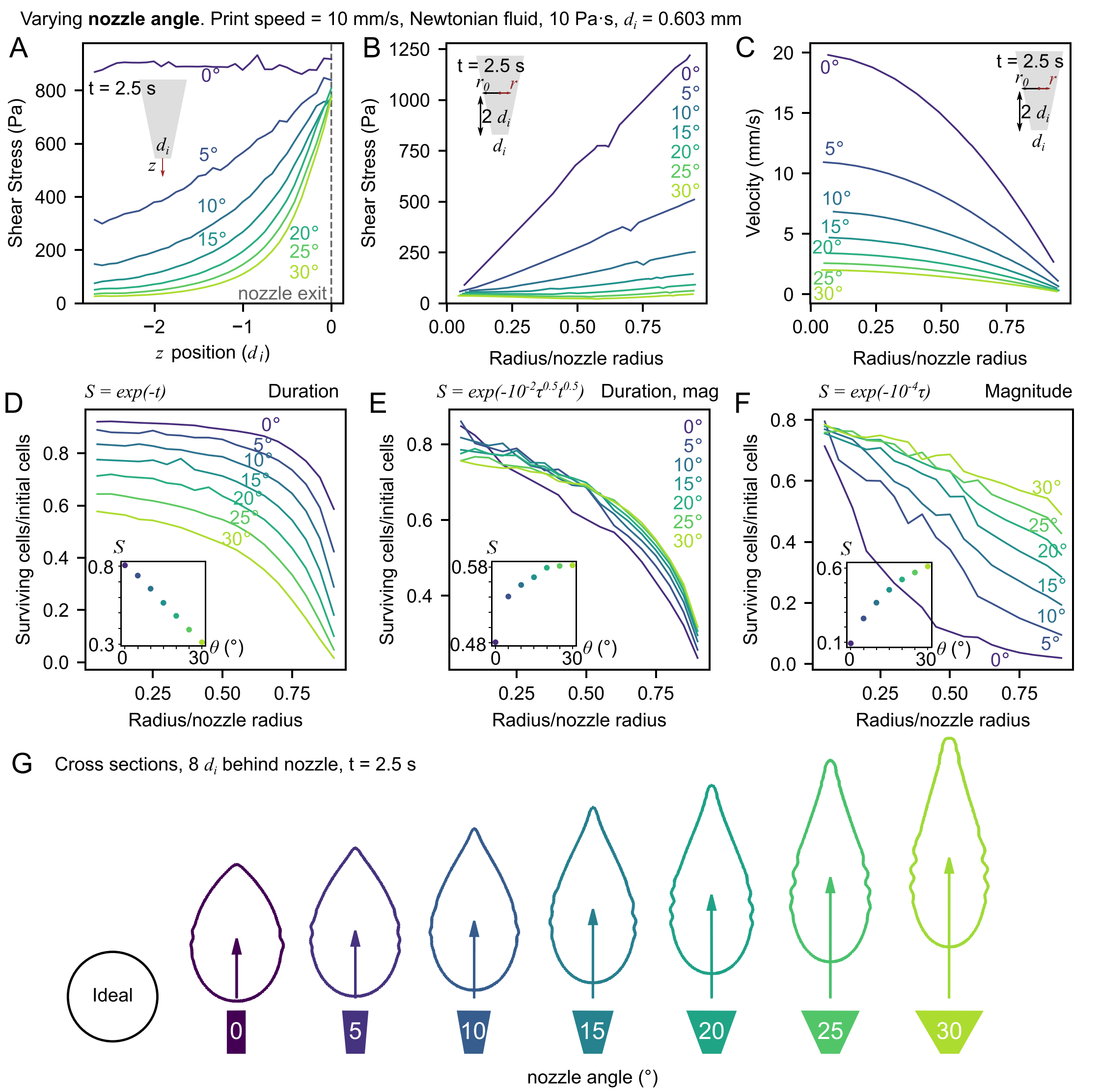

FIG. 4. The effect of nozzle angle on stresses and morphologies in Newtonian fluids, with $\eta = 1$ Pa · s, at a print speed of 10 mm/s, after 2.5 s of flow. (a) Average shear stress across the nozzle-cross section as a function of z position along the length of the nozzle. (b) and (c) Line traces $2d_i$ above the nozzle exit across the diameter of the nozzle. (b) Shear stress as a function of radial position. (c) Velocity magnitude as a function of radial position. (d)–(f) Fraction of surviving cells as a function of radial position, for varying nozzle angles, given three different models. Inset indicates survival for all cells in the nozzle, as a function of nozzle angle. (d) Survival depends only on duration of stress. (e) Survival depends equally on magnitude and duration. (f) Survival only depends on magnitude of stress. (g) Cross-sections of extruded filaments $8d_i$ behind the nozzle. Arrows indicate the displacement between the intended center and calculated centroid of the cross section.

the nozzle, and thus, less vertical compression of the filament [Fig. 5(g)]. The effect is similar in Newtonian fluids. For a cylindrical nozzle in a Newtonian fluid, the displaced support flows in plane around the nozzle [Fig. 5(h)]. With increasing nozzle angle, more fluid is displaced downward, leading to downward flows along the sides of the nozzle that are matched by upward flows behind the nozzle [Fig. 5(h)]. These upward flows push the filament upward, where the filaments are compressed horizontally and elongated vertically by converging support flows.

Varying the nozzle diameter can change survival rates and filament morphologies. Here, we investigate four sizes of nozzle: 18 gauge ($d_i = 0.838$, $t_w = 0.216$ mm), 20 gauge ($d_i = 0.603$, $t_w = 0.152$ mm), 22 gauge ($d_i = 0.413$, $t_w = 0.152$ mm), and 25 gauge ($d_i = 0.26$, $t_w = 0.127$ mm). We expand the simulated region to scale with the inner diameter of the nozzle, but the print speed remains the same. As the nozzles grow bigger, they have larger inner diameter to outer diameter ratios, as shown in Fig. 6(g). For both cylindrical nozzles and 15° conical nozzles, as the diameter increases, the average shear stress across the nozzle decreases [Figs. 6(a) and S16(a)]. The average stress decreases because as the diameter increases, the shear stress at the wall decreases considerably, and the shear stress at the center of the nozzle decreases slightly [Figs. 6(b) and S16(b)]. However, the velocity profile

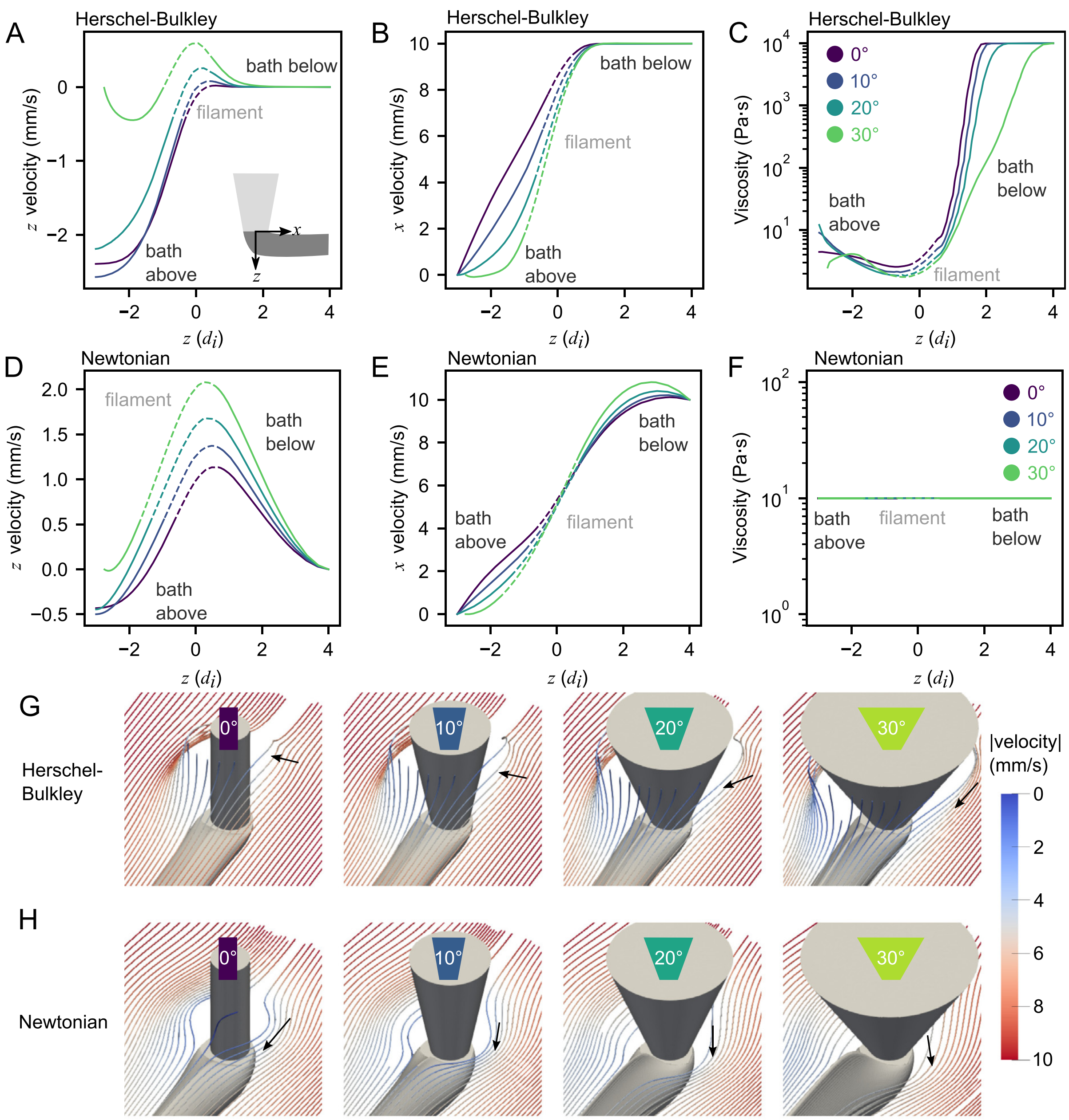

FIG. 5. Simulations at print speeds of 10 mm/s with a d_i of 0.603 mm. (a)–(f) Line profiles 1.4 mm downstream of the nozzle, after 2.5 s of flow, as a function of vertical z position in the bath. (a) and (d) Vertical velocity in the z direction, (b) and (e) Horizontal velocity in the x direction, and (c) and (f) Fluid viscosity, for (a)–(c) Herschel–Bulkley and (d)–(f) Newtonian inks and supports. (g) and (h) Streamlines around the nozzle and filament after 2.5 s of flow, colored by velocity magnitude, for (g) Herschel–Bulkley and (h) Newtonian fluids. Black arrow indicates the part of the flow field that either sweeps upward or downward, depending on nozzle angle and rheology.

does not change with diameter [Figs. 6(c) and S16(c)]. In these simulations, the nozzle length scales with the nozzle diameter. As a result, because the fluid is flowing at the same speed through a longer nozzle, it spends more time in the larger nozzles. Thus, when cell survival depends only on duration, increasing the nozzle length decreases survival rates across the entire nozzle width [Figs. 6(d) and S16(d)]. The same is true when cell survival depends equally on duration and magnitude [Figs. 6(e) and S16(e)]. If the nozzle was merely wider, but not longer, the duration would be the same, so duration-controlled cell survival would not be impacted by the nozzle diameter. Where the cell survival depends only on stress magnitude, increasing the nozzle diameter improves survival across the entire nozzle [Figs. 6(f) and S16(f)].

In Herschel–Bulkley fluids, increasing the nozzle diameter leads to slightly taller, more pointed filaments with a larger vertical

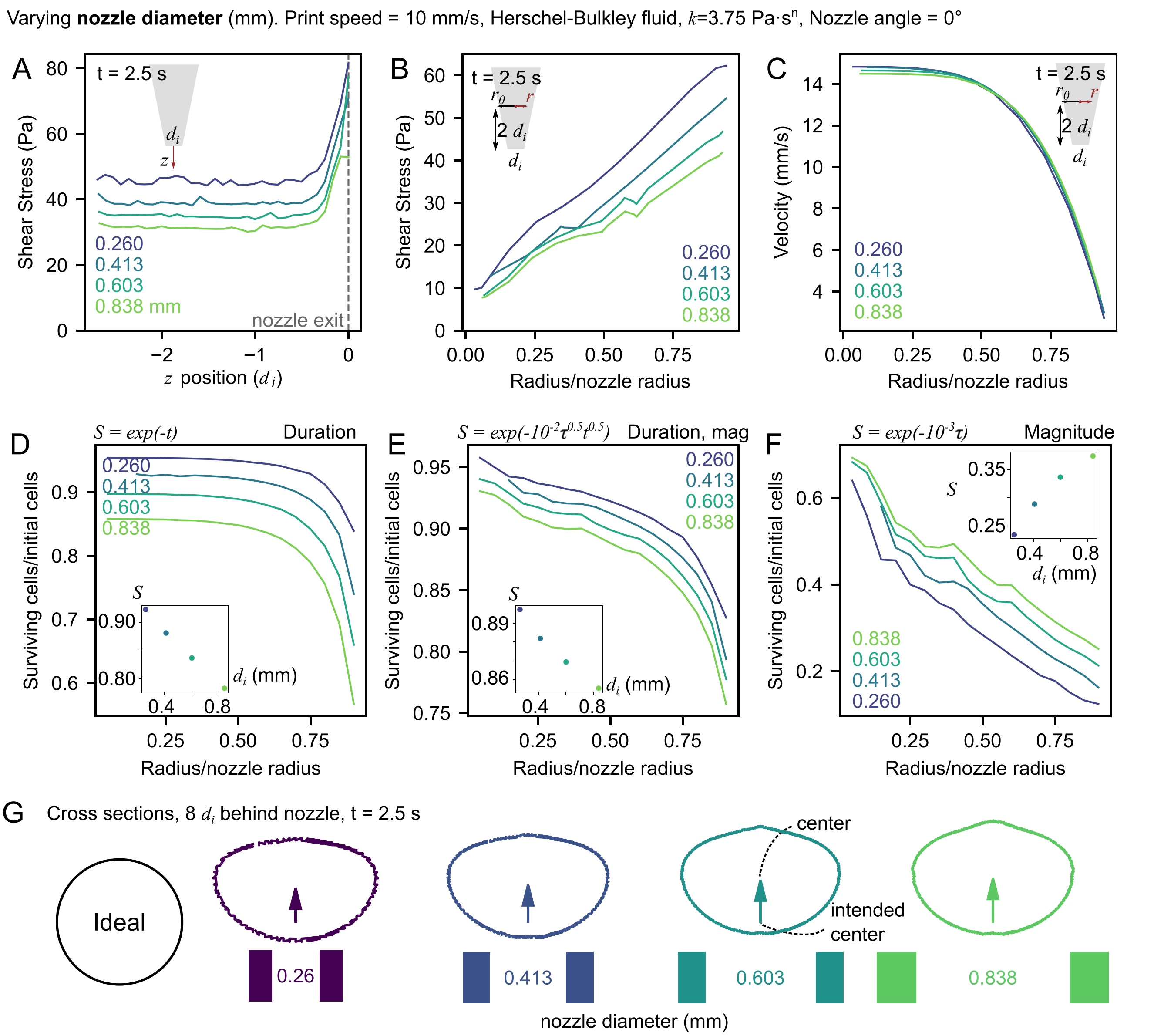

FIG. 6. The effect of nozzle diameter on stresses and morphologies in Herschel–Bulkley fluids, with $k = 3.75\,\mathrm{Pa \cdot s}^n$, with a nozzle angle of 0°, at a print speed of 10 mm/s, after 2.5 s of flow. (a) Average shear stress across the nozzle-cross section as a function of z position along the length of the nozzle. (b) and (c) Line traces $2d_i$ above the nozzle exit across the diameter of the nozzle. (b) Shear stress as a function of radial position. (c) Velocity magnitude as a function of radial position. (d)–(f) Fraction of surviving cells as a function of radial position, for varying print speed, given three different models. Inset indicates survival for all cells in the nozzle, as a function of print speed. (d) Survival depends only on duration of stress. (e) Survival depends equally on magnitude and duration. (f) Survival only depends on magnitude of stress. (g) Cross-sections of extruded filaments $8d_i$ behind the nozzle. Arrows indicate the displacement between the intended center and calculated centroid of the cross section.

shift [Figs. 6(g) and S16(g)]. However, these differences are small: a 12% increase in aspect ratio for the cylindrical nozzle and an 8% increase in aspect ratio for the 15° conical nozzle, from a fourfold increase in diameter. If the print speeds are scaled proportionally to the nozzle inner diameter, such that the larger nozzle has faster flow and the smaller nozzle has slower flow, the nozzle diameter has a much smaller impact on the filament aspect ratio [Fig. S20(b)]. If the ink and support are Newtonian, the diameter has no effect on the filament cross-sectional shape, regardless of whether the print speeds are constant or scaled relative to the diameter [Fig. S20(b)]. Increasing the nozzle diameter while maintaining a constant print speed shrinks the yielded zone within the support [Fig. S20(c)]. Increasing the nozzle diameter while scaling the print speed relative to the nozzle diameter shrinks the yielded zone by a much smaller amount.

The evolution of the filament shape over time depends on nozzle diameter. For Herschel–Bulkley fluids, the tip of the filament is flat and wide, as shown in Ref. 20 and Fig. 7. The filament cross-section then becomes tall and narrow. The height peaks, and then the filaments become shorter and wider (Fig. 7). At larger nozzle diameters, it takes longer to reach the short and wide quasi-steady-state cross-sectional shape. As a result, the cross-section collected at 2.5 s, $8d_i$ downstream of the nozzle, is taller and narrower than the steady-state condition for the largest nozzle. Because the cross-section evolution in Fig. 7 is collected at a constant speed, this means that the larger nozzle experiences longer transients at the start of an extruded line, relative to the filament diameter and in absolute time, than the smaller nozzles.

When the ink and support are identical, changing the print speed does not change the filament morphology, but it can worsen or improve cell survival. Here, the ink speed and support speed are equal, where the ink speed is the ink flux divided by the cross-sectional area of the outlet. In both cylindrical and 15° conical nozzles, increasing the print speed increases the shear stress uniformly along the length of the nozzle [Figs. 8(a) and S21(a)]. In cylindrical nozzles, this is largely due to an increase in shear stress at the nozzle walls at higher print speeds, relating to a faster shear rate [Fig. 8(b)]. At the center of the nozzle, the shear stress is only slightly higher at faster speeds [Fig. 8(b)]. In conical nozzles, the stress increases more uniformly along the radius of the nozzle [Fig. S21(b)]. In cylindrical nozzles, plug flow is maintained within the nozzle for all print speeds, but increasing the overall print speed narrows the plug and increases the velocity of the plug [Fig. 8(c)]. In conical nozzles, increasing the print speed increases the velocity at the center of the nozzle [Fig. S21(c)].

Depending on the survival model, increasing the print speed can worsen or improve survival. If the cells depend only on the duration of stress, increasing the flow rate decreases the amount of time the plug spends in the nozzle, improving survival [Figs. 8(d) and S21(d)]. If the cells depend equally on the duration and magnitude of stress, survival still improves at higher print speeds [Figs. 8(e) and S21(e)]. Where the cells depend only on stress magnitude, slowing the flow rate improves cell survival by decreasing the rate of cell damage toward the nozzle wall [Figs. 8(f) and S21(f)].

Keeping the ink velocity equal to the support velocity, and using an identical ink and support, increasing the print speed does not change the cross-sectional shape [Figs. 8(g) and S21(g)]. The shape of the filament experiences transients, where the cross-section changes along the length of the filament.[20] As a result, at low print speeds, less filament has been extruded after 2.5 s [Figs. S24 and S21(h)], leading to slight transient effects in the cross-sectional shape in Figs. 8(g) and S21(g).

The local viscosities of the ink and support in the extrusion region influence cell survival and the filament shape.[20,24] There are multiple ways to alter the simulated local viscosity. One could alter the

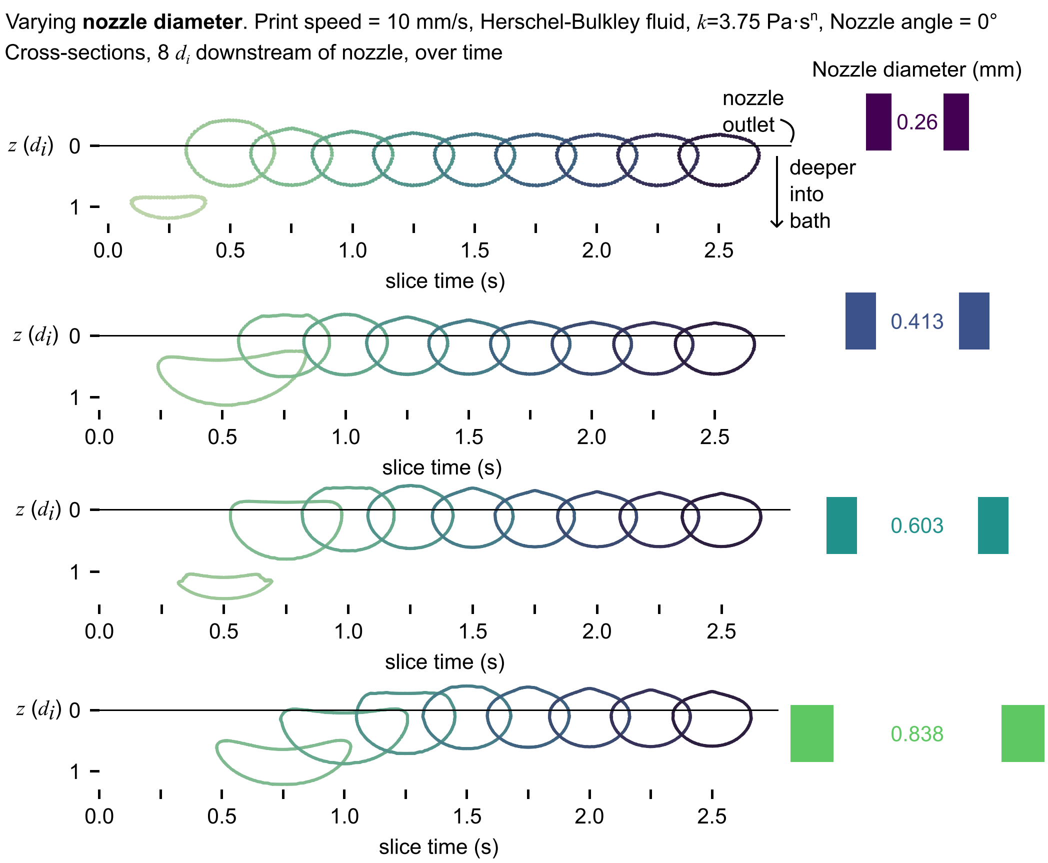

FIG. 7. Evolution of filament cross sections over time, for varying nozzle diameter, in Herschel–Bulkley fluids, with $k = 3.75\,\mathrm{Pa \cdot s}^n$, with a nozzle angle of 0°, at a print speed of 10 mm/s.

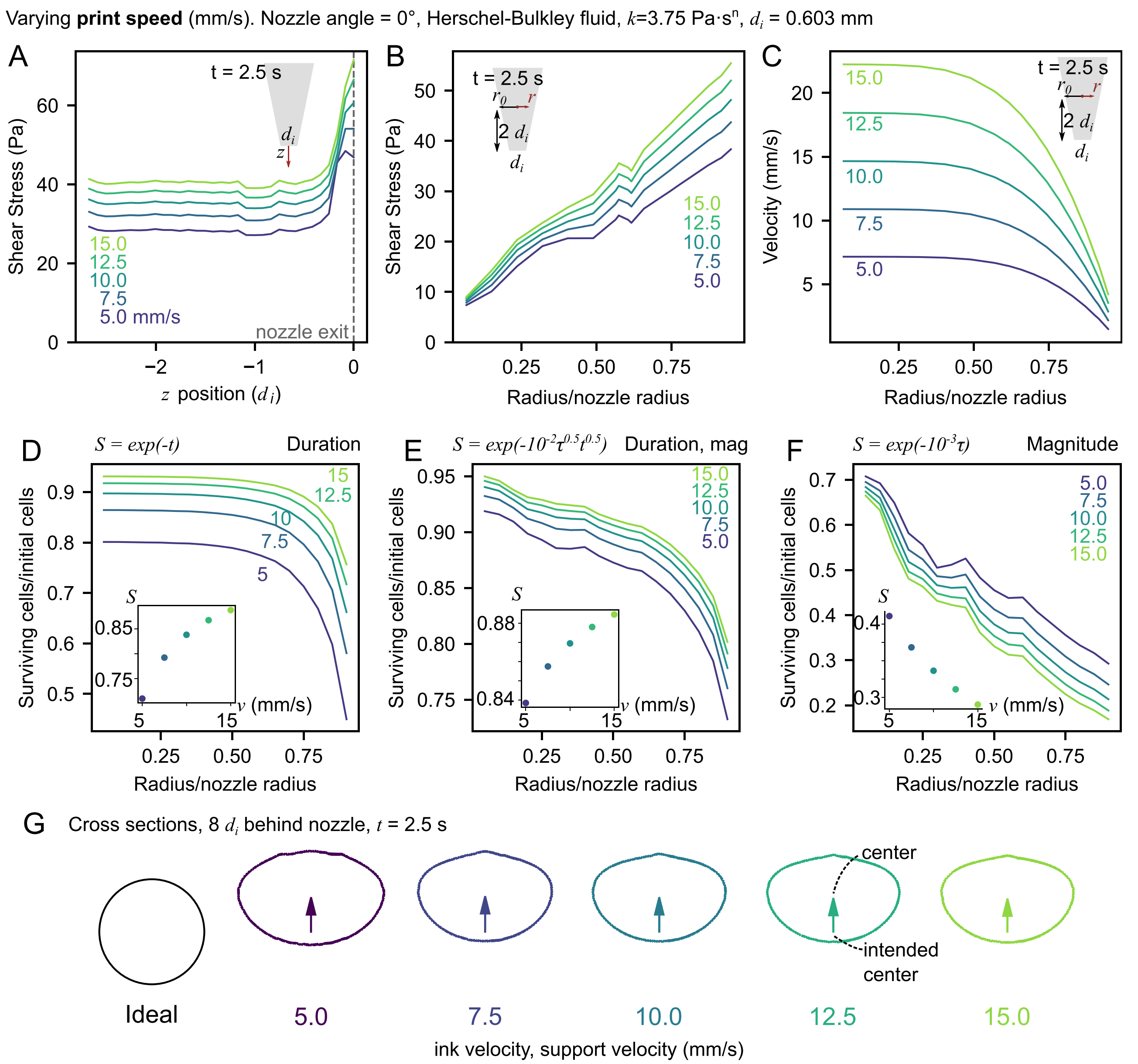

FIG. 8. The effect of print speed on stresses and morphologies in Herschel–Bulkley fluids, with $k = 3.75\,\mathrm{Pa} \cdot \mathrm{s}^n$, with a nozzle angle of 0°, after 2.5 s of flow. The stage translation speed is set equal to the flux of ink at the nozzle exit, divided by the area of the nozzle exit. (a) Average shear stress across the nozzle-cross section as a function of z position along the length of the nozzle. (b) and (c) Line traces $2d_i$ above the nozzle exit across the diameter of the nozzle. (b) Shear stress as a function of radial position. (c) Velocity magnitude as a function of radial position. (d)–(f) Fraction of surviving cells as a function of radial position, for varying print speed, given three different models. Inset indicates survival for all cells in the nozzle, as a function of print speed. (d) Survival depends only on duration of stress. (e) Survival depends equally on magnitude and duration. (f) Survival only depends on magnitude of stress. (g) Cross-sections of extruded filaments $8d_i$ behind the nozzle. Arrows indicate the displacement between the intended center and calculated centroid of the cross section.

viscosities of Newtonian inks and supports or one could alter the several parameters in the Herschel–Bulkley model. Previous simulations in cylindrical nozzles indicated that in Newtonian fluids, if the viscosity ratio is constant, the filament cross-section does not change [replotted in Fig. 9(g)], and in Herschel–Bulkley fluids, if the yielded part of the viscosity–strain rate curve is constant, the filament cross-section does not change with plateau viscosity η_0.[20] Similarly, previous experiments indicated that at constant surface tension and nozzle diameter but with varying ink and support compositions, extrusion speed, and stage speed, the cross-sectional aspect ratio scales with the local

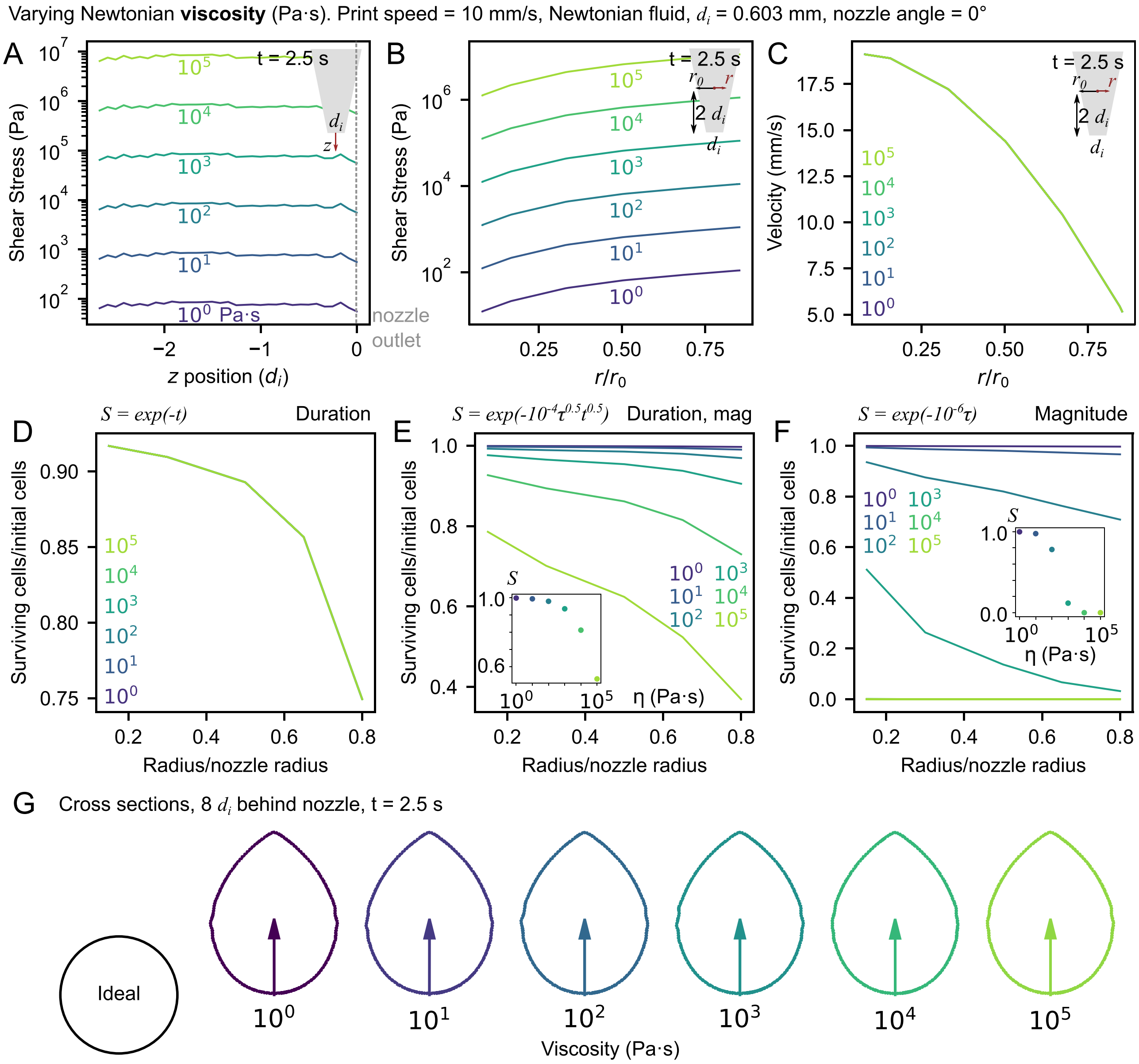

FIG. 9. The effect of Newtonian viscosity on stresses and morphologies, with a nozzle angle of 0°, an inner diameter d_i of 0.603 mm at a print speed of 10 mm/s, after 2.5 s of flow. The 1000 Pa s sample is collected at 5 s. The ink and support viscosities are equal. (a) Average shear stress across the nozzle-cross section as a function of z position along the length of the nozzle. (b) and (c) Line traces $2d_i$ above the nozzle exit across the diameter of the nozzle. (b) Shear stress as a function of radial position. (c) Velocity magnitude as a function of radial position. (d)–(f) Fraction of surviving cells as a function of radial position, for varying print speed, given three different models. Inset indicates survival for all cells in the nozzle, as a function of print speed. (d) Survival depends only on duration of stress. (e) Survival depends equally on magnitude and duration. (f) Survival only depends on magnitude of stress. (g) Cross-sections of extruded filaments $8d_i$ behind the nozzle. Arrows indicate the displacement between the intended center and calculated centroid of the cross section.

viscosity ratio, defined where the support shear rate is the support velocity divided by the nozzle outer diameter, and the ink shear rate is the ink velocity divided by the nozzle inner diameter.[24]

For simplicity, first consider the effect of viscosity in Newtonian fluids. In agreement with the analytical solution (Fig. S6), increasing the Newtonian ink viscosity by a factor of 10 increases the shear stress in the nozzle by a factor of 10 [Figs. 9(a) and 9(b)], but it does not change the velocity profile within the nozzle in Newtonian fluids [Fig. 9(c)]. As a result, when cell survival depends only on duration, the Newtonian ink viscosity does not influence cell survival [Fig. 9(d)]. When cell survival depends on the stress magnitude, increasing the ink viscosity decreases survival rates, particularly at the nozzle walls

[Figs. 9(e) and 9(f)]. Even in conical nozzles, for Newtonian fluids, increasing the viscosity but keeping the viscosity ratio constant does not change the cross-sectional shape [Figs. 9(g) and S25].

Because there are more parameters involved, Herschel–Bulkley fluids have more complicated behaviors. For Herschel–Bulkley fluids, altering the consistency index k can change both the cross-sectional shape and the shear stresses, even though k is the same for the ink and support. Increasing k uniformly increases the viscosity of the final yielded portion of the viscosity–shear rate curve, leading to higher local viscosities [Fig. S26(i)]. Like in Newtonian fluids, in Herschel–Bulkley fluids, the stress inside the nozzle increases with increasing consistency index, both along the length of the nozzle and across the width of the nozzle [Figs. S26(a) and S26(b)]. With increasing k, the plug flow region in the center of the nozzle narrows and becomes faster, and the ink near the wall becomes slower [Fig. S26(c)]. In Herschel–Bulkley fluids, regardless of the survival function, increasing k worsens survival. For duration-sensitive cells, increasing k improves survival at the center of the nozzle but worsens it at the edge [Fig. S26(d)]. Otherwise, increasing k worsens survival throughout the nozzle [Figs. S26(e) and S26(f)]. Thus, increasing the local ink viscosity within the nozzle via the consistency index k will always be harmful to cells. Increasing k can also alter the filament morphology. Where $\eta_0 = 10^4$ Pa · s, $\tau_0 = 10$ Pa, and $n = 0.45$, increasing k leads to taller, sharper filaments.

IV. DISCUSSION

A. Morphology

In previous papers, we established that for a constant nozzle geometry, the morphology of filaments extruded into a support bath depends primarily on the viscosity ratio and the capillary number.[20,24] Here, we showed that the nozzle geometry can also influence the filament morphology, beyond its effects on the viscosity ratio. Where the nozzle geometry is constant, the cross-sectional height/width decreases with increasing local ink viscosity/support viscosity.[20,24] The increase in aspect ratio with increasing nozzle angle could be attributed to a decrease in viscosity ratio, if the local viscosity of the ink is defined using the inner nozzle diameter at the outlet and the local viscosity of the support is defined using the outer nozzle diameter above the outlet, where the local shear rate is defined as the programed speed divided by the diameter. A larger conical nozzle angle would increase the diameter, and thus, decrease the shear rate on the support, leading to a more viscous support [Fig. S29(a)]. However, because the nozzle angle also changes the aspect ratio of filaments in Newtonian fluids, despite maintaining a constant viscosity ratio [Fig. S29(d)], these changes in aspect ratio cannot be simply explained by the change in viscosity ratio. Moreover, in Herschel–Bulkley fluids the local viscosity of the support near the filament does not change with nozzle angle, although the size of the yielded zone increases with nozzle angle (Fig. S11). As such, the shape of the flow field, as dictated by volume displacement, is necessary to explain the effect of nozzle angle on the filament morphology. The shape of the flow field may also explain the ridges that appear on the side of the filament. The convergence of upward-flowing support and support flowing in plane downstream of the nozzle may lead to buckling of the ink–support interface. Alternatively, stronger converging flows could cause the growth of perturbations at the ink–support interface, leading to persistent ridges on the filament surface. While surface roughness on filaments has been documented in embedded 3D printing,[24] ridges along the length of the filament have not been documented, so these ridges could be a simulation artifact.

The aspect ratio slightly increases with nozzle diameter. As one incorrect explanation, because the wall thickness was set to commercial nozzle sizes rather than remaining constant relative to the inner nozzle diameter, the change in relative shear rate between the inner and outer diameter could lead to a change in viscosity ratio, which would lead to a change in aspect ratio in accordance with previous findings. However, if we calculate the shear rates using the outlet inner and outer diameters, we find that the viscosity ratio does not increase monotonically with nozzle diameter [Fig. S29(b)]. Moreover, for Herschel–Bulkley fluids, the aspect ratio increases with increasing local viscosity ratio, which is the opposite direction of the trend determined for constant nozzle geometry [Fig. S29(b)]. This was also true for the conical nozzles, but conical nozzles change the shape of the flow field. Examining the velocity field, the shape of the flow field around the nozzle is largely unaffected by the nozzle diameter [Fig. S20(a)]. For diameter sweeps, the small nozzles producing shorter aspect ratios have a larger yielded zone [Fig. S20(c)]. However, in previous simulations, a larger yielded zone correlated with a sharper top edge,[20] and for the nozzle angle sweeps, a larger yielded zone correlated with a taller aspect ratio. Ultimately, transients best explain the trend in diameter. We scaled the dimensions of the simulated volume by the inner diameter of the nozzle. The bath is initialized with a starting velocity of 0 mm/s in the bulk and 10 mm/s on the upstream, bottom, left, and right faces of the simulated volume. As a result, there are transients in velocity within the bath, and it takes a finite amount of time for the bulk of the bath to reach a steady state velocity.[20] In a larger bath, the transients take longer. As a result, the larger nozzle takes longer to reach its short, wide steady state cross-sectional shape and is taller and narrower than the cross sections produced by the smaller nozzles. However, if the print speed is scaled by the nozzle diameter, the faster speed at the walls compensates for the larger bath and shortens the transients in the larger nozzle, leading to smaller changes in filament aspect ratio with nozzle diameter. Regardless of the reasons for the change in a cross-sectional shape with the nozzle diameter, the aspect ratio increases by 12% with a fourfold increase in inner diameter, while the average stress decreases by 31%. Thus, the improvement in cell survival may be worth the small increase in shape defects and loss of resolution.

The increase in aspect ratio with Herschel–Bulkley consistency index serves more as a thought experiment than a practical course of action. In real materials, rheology is typically altered via composition and processing, which alter the behavior of the materials above and below yield, typically increasing the yield stress and local viscosities simultaneously. Previous experiments showed that the cross-sectional shape of the filament can largely be controlled via the local viscosities of the ink and support, for zero surface tension systems, and for non-zero surface tension systems, the cross-sectional shape correlates with the capillary number $Ca = v_{ink}\eta_{sup}/\sigma$, where v_{ink} is the flow speed, η_{sup} is the local support viscosity, and σ is the surface tension.[24] In this work, only a single component of the yielded behavior is controlled, and the results indicate that neither the local viscosities nor the yield stresses alone can predict the filament shape in these theoretical materials. More work is necessary to extricate whether these k effects are specific to the implementation of the Herschel–Bulkley model in

TABLE I. Summary of the effects on aspect ratio, stress duration-dependent damage, and stress magnitude-dependent damage. HB: Herschel Bulkley, Newt: Newtonian, ↑: increase, ↓: decrease, 0: no effect. η: viscosity, and k: consistency index. *only if the length remains constant.

Treatment	Aspect ratio	Damage in duration-sensitive cells	Damage in magnitude-sensitive cells
↑ Nozzle angle	↑	↑	↓
↑ Nozzle diameter	HB ↑, Newt 0	0^*	↓
↓ Print speed	0	↑	↓
↓ Newt η	0 if η_{ink}/η_{sup} is constant	0	↓
↓ HB k	↓	↓	↓

OpenFOAM, and how the different components of the model influence filament morphology. More practically, we know from these Herschel–Bulkley and Newtonian simulations that decreasing the viscosity of the ink and support can be beneficial for cell survival.

B. Survival

In the bioprinting literature, cell damage has been proposed to depend on the magnitude of shear stresses imposed on cells inside the nozzle.[6,45] Other models have proposed that damage depends on both the duration and magnitude of stress.[8,11] This work confirms the stress magnitude dependencies on nozzle angle, nozzle diameter, print speed, and viscosity which were discussed in other works analytically and experimentally.[3,5,6,9,12–16] However, we find that several of the strategies that decrease shear stresses also increase the duration of time the cells spend inside the nozzle. As such, in bioprinting applications, the damage mitigation strategies employed should be tailored to whether the cell survival depends more on the magnitude or duration of stress. If the duration matters more, a smaller nozzle angle, shorter nozzle length, faster extrusion speed, and potentially higher consistency index k should be used. If the stress magnitude matters more, a larger nozzle angle, larger nozzle diameter, slower extrusion speed, and lower ink viscosity should be used. If both matter, a large diameter or lower viscosity may be more beneficial, preventing the duration-dependent damage from canceling out the magnitude-dependent damage. Notably, other works have demonstrated improvement in cell viability with these magnitude-centered strategies,[3,5,9,12,14,15] suggesting that many cells are more sensitive to stress magnitude than the stress duration.

V. CONCLUSIONS

In this work, we examined the effect of four stress mitigation strategies on cell survival and filament morphology in embedded ink writing. Increasing the nozzle angle, increasing the nozzle diameter, decreasing the print speed, and decreasing the ink viscosity decrease damage in cells that are sensitive to the magnitude of stress. Decreasing the nozzle angle, decreasing the nozzle length, increasing the print speed, and decreasing the Herschel–Bulkley consistency index decrease damage in cells that are sensitive to the duration of stress. Most cells are sensitive to both the magnitude and duration of cell damage. One should first measure how the cell damage scales with magnitude and duration before choosing a strategy, to improve cell survival. Because most reports indicate that cell survival improves with increasing nozzle angle and nozzle diameter and decreasing print speed, it is likely that most cells are more sensitive to the shear stress magnitude than the duration. One should also consider the repercussions for the extruded filament morphology. Increasing the nozzle angle, increasing the nozzle diameter in Herschel–Bulkley fluids, and increasing the Herschel–Bulkley consistency index can lead to taller, narrower filaments with a sharp top edge, which could lead to surface roughness, porosity, poor adhesion between filaments, and anisotropic functional and mechanical properties in the final part.

Each of the strategies has practical limitations, in addition to the changes in performance listed in Table I. While we show that conical nozzles displace fluid vertically, leading to larger filament aspect ratios, they may also limit toolpaths to in-plane, bottom-up printing, because the larger displaced volume could disrupt existing structures. Moreover, there is a practical limit to how large the nozzle angle can be, depending on how deep the print bath is, and how the nozzle connects to the ink reservoir. There are similar practical limits on the nozzle diameter. Additionally, larger transients in large nozzles may harm print fidelity. While decreasing the print speed improves viability, it also increases the printing time, leading to low throughput and potential harm to cells that may settle or be starved for nutrients in the ink reservoir.

While rheology is a potent tool for improving survival, there are limitations on its use. First, while a lower-viscosity ink lowers the shear stress on cells, the viscosity often correlates with the stiffness and yield strength of the crosslinked material, which provide important mechanical signals to proliferating and differentiating cells.[5] Second, rheological control is not limited to the ink matrix. The rheology of cell-laden inks is strongly influenced by the cell concentration and cell viability, but the correlation is non-monotonic.[6,7] A high concentration of cells is necessary for development of tissues.[5] As such, the concentration of cells limits the range of viscosities allowable for a certain application. It has been proposed that because non-Newtonian fluids can achieve plug flow, they can reduce the shear stress on cells compared to Newtonian fluids.[46] Additionally, models of inkjet printing indicated that viscoelastic fluids better protect cells from impact than Newtonian fluids.[47] In these simulations, plug flow is only achieved within the cylindrical nozzle in Herschel–Bulkley fluids. Confirming the proposal, the plug flow region at the center of the cylindrical nozzle achieves a lower minimum stress than the conical nozzles, despite the faster velocity of the plug [Figs. 3(b) and 3(c)]. Widening of the plug flow region via decreased ink flow rate also correlates with lower shear stresses, but those lower shear stresses largely have to do with the lower shear rates at lower print speeds [Figs. 8(b) and 8(c)].

The higher rate of cell damage at the nozzle wall presents both opportunities and challenges. Additionally, because shear stresses are higher on the downstream edge of the nozzle outlet than the upstream edge, more cells will be damaged on the top surface of the filament than the bottom surface. Active positioning methods such as acoustophoresis could improve the survival rate by moving cells to the center of the nozzle, where shear stresses and durations are lower.[48,49] Shear-induced migration could induce a more modest improvement in survival.[50] Alternatively, the flow profile for both Newtonian and non-Newtonian fluids could be altered by allowing slip at the nozzle wall via surface modification. With or without active positioning, extrusion will result in a lack of viable cells at the filament surface, and thus, the interfaces between filaments. This could lead to variations in mechanical properties throughout the part due to uneven distribution of cells.[6,7,46] Cell remodeling of the ink matrix and deposition of extracellular matrix also alter the mechanical properties of the construct, so a lack thereof at the filament surface would lead to variations in mechanical properties. These variations could be leveraged to mimic the anisotropy inherent to many living tissues. Alternatively, strategies for encouraging homogenization and migration of cells throughout the part post-extrusion could be employed.

Damage can also occur within the bath after the cells have left the nozzle, due to stresses that the nozzle imposes on the surrounding fluid during translation. A high-stress peak occurs on the outer edge of the nozzle outlet, which is not counted in these survival calculations, but would lead to additional cell damage on the top surface of the filament. While the cells experience non-zero stresses after extrusion, these stresses are much lower than the stresses inside the nozzle, so the vast majority of damage takes place inside the nozzle. Additionally, while this work did not examine extensional flows, considerable extension can occur whenever there is a transition in tubing or a sudden contraction within the nozzle.[5,22] Of course, one could avoid cell damage within the nozzle by printing a scaffold and seeding cells onto the printed structure. However, this could lead to lower cell migration into the structure and poor exchange of metabolites between the cells and the medium.[3,5] Alternatively, chemical and mechanical preconditioning of the ink can help to prepare cells for the high shear stresses experienced during the printing process.[5]

SUPPLEMENTARY MATERIAL

See the supplementary material for survival model; analytical solutions; methodological refinement; shear stress and viscosity maps; stress, survival, and shape metrics for conical nozzles and Herschel–Bulkley consistency index; flow field shapes; trends with respect to viscosity ratio.

ACKNOWLEDGMENTS

This work was supported by the National Research Council postdoctoral fellowship and the National Institute of Standards and Technology Summer Undergraduate Research Fellowship.

AUTHOR DECLARATIONS

Conflict of Interest

The authors have no conflicts to disclose.

Author Contributions

Leanne M. Friedrich: Conceptualization (equal); Data curation (equal); Formal analysis (equal); Investigation (equal); Methodology (equal); Software (equal); Supervision (equal); Visualization (equal); Writing – original draft (equal). **Ross T. Gunther:** Data curation (equal); Investigation (equal); Methodology (equal); Software (equal); Visualization (equal); Writing – review & editing (supporting). **Jonathan Seppala:** Resources (lead); Supervision (equal); Writing – review & editing (equal).

DATA AVAILABILITY

The data that support the findings of this study are openly available in NIST Public Data at http://doi.org/10.18434/mds2-2602 (Ref. 37) and in NIST Public Data at http://doi.org/10.18434/mds2-2604 (Ref. 39).

REFERENCES

[1] I. T. Ozbolat and M. Hospodiuk, "Current advances and future perspectives in extrusion-based bioprinting," Biomaterials **76**, 321–343 (2016).
[2] C. S. O'Bryan, T. Bhattacharjee, S. R. Niemi, S. Balachandar, N. Baldwin, S. T. Ellison, C. R. Taylor, W. G. Sawyer, and T. E. Angelini, "Three-dimensional printing with sacrificial materials for soft matter manufacturing," MRS Bull. **42**, 571–577 (2017).
[3] L. Ning and X. Chen, "A brief review of extrusion–based tissue scaffold bio–printing," Biotechnol. J. **12**, 1600671 (2017).
[4] E. Mirdamadi, N. Muselimyan, P. Koti, H. Asfour, and N. Sarvazyan, "Agarose slurry as a support medium for bioprinting and culturing freestanding cell-laden hydrogel constructs," 3D Print. Addit. Manuf. **6**, 158–164 (2019).
[5] S. Boularaoui, G. Al Hussein, K. A. Khan, N. Christoforou, and C. Stefanini, "An overview of extrusion-based bioprinting with a focus on induced shear stress and its effect on cell viability," Bioprinting **20**, e00093 (2020).
[6] A. Blaeser, D. F. Duarte Campos, U. Puster, W. Richtering, M. M. Stevens, and H. Fischer, "Controlling shear stress in 3D bioprinting is a key factor to balance printing resolution and stem cell integrity," Adv. Healthcare Mater. **5**, 326–333 (2016).
[7] L. Ning, A. Guillemot, J. Zhao, G. Kipouros, and X. Chen, "Influence of flow behavior of alginate-cell suspensions on cell viability and proliferation," Tissue Eng., Part C **22**, 652–662 (2016).
[8] M. Li, X. Tian, N. Zhu, D. J. Schreyer, and X. Chen, "Modeling process-induced cell damage in the biodispensing process," Tissue Eng., Part C **16**, 533–542 (2010).
[9] M. Li, X. Tian, D. J. Schreyer, and X. Chen, "Effect of needle geometry on flow rate and cell damage in the dispensing–based biofabrication process," AIChE J. **27**, 1777–1784 (2011).
[10] R. Paul, J. Apel, S. Klaus, F. Schügner, P. Schwindke, and H. Reul, "Shear stress related blood damage in laminar Couette flow," Artif. Organs **27**, 517–529 (2003).
[11] L. Ning, N. Betancourt, D. J. Schreyer, and X. Chen, "Characterization of cell damage and proliferative ability during and after bioprinting," ACS Biomater. Sci. Eng. **4**, 3906–3918 (2018).
[12] J. Emmermacher, D. Spura, J. Cziommer, D. Kilian, T. Wollborn, U. Fritsching, J. Steingroewer, T. Walther, M. Gelinsky, and A. Lode, "Engineering considerations on extrusion-based bioprinting: Interactions of material behavior, mechanical forces and cells in the printing needle," Biofabrication **12**, 025022 (2020).
[13] G. Gao, B. S. Kim, J. Jang, and D.-W. Cho, "Recent strategies in extrusion-based three-dimensional cell printing toward organ biofabrication," ACS Biomater. Sci. Eng. **5**, 1150–1169 (2019).
[14] T. Billiet, E. Gevaert, T. De Schryver, M. Cornelissen, and P. Dubruel, "The 3D printing of gelatin methacrylamide cell-laden tissue-engineered constructs with high cell viability," Biomaterials **35**, 49–62 (2014).
[15] R. Chang, J. Nam, and W. Sun, "Effects of dispensing pressure and nozzle diameter on cell survival from solid freeform fabrication-based direct cell writing," Tissue Eng., Part A **14**, 41–48 (2008).
[16] N. Chen, K. Zhu, Y. S. Zhang, S. Yan, T. Pan, M. Abudupataer, G. Yu, M. F. Alam, L. Wang, X. Sun, Y. Yu, C. Wang, and W. Zhang, "Hydrogel bioink with multilayered interfaces improves dispersibility of encapsulated cells in extrusion bioprinting," ACS Appl. Mater. Interfaces **11**, 30585–30595 (2019).
[17] A. M. Compaan, K. Song, W. Chai, and Y. Huang, "Cross-linkable microgel composite matrix bath for embedded bioprinting of perfusable tissue constructs and sculpting of solid objects," ACS Appl. Mater. Interfaces **12**, 7855 (2020).
[18] S. R. Moxon, M. E. Cooke, S. C. Cox, M. Snow, L. Jeys, S. W. Jones, A. M. Smith, and L. M. Grover, "Suspended manufacture of biological structures," Adv. Mater. **29**, 1605594 (2017).

[19]L. Ning, R. Mehta, C. Cao, A. Theus, M. Tomov, N. Zhu, E. R. Weeks, H. Bauser-Heaton, and V. Serpooshan, "Embedded 3D bioprinting of gelatin methacryloyl-based constructs with highly tunable structural fidelity," ACS Appl. Mater. Interfaces **12**, 44563–44577 (2020).
[20]L. M. Friedrich and J. E. Seppala, "Simulated filament shapes in embedded 3D printing," Soft Matter **17**, 8027 (2021).
[21]A. Shapira, N. Noor, H. Oved, and T. Dvir, "Transparent support media for high resolution 3D printing of volumetric cell-containing ECM structures," Biomed. Mater. **15**, 045018 (2020).
[22]H. Ding and R. Chang, "Printability study of bioprinted tubular structures using liquid hydrogel precursors in a support bath," Appl. Sci. **8**, 403 (2018).
[23]T. Calais, N. D. Sanandiya, S. Jain, E. V. Kanhere, S. Kumar, R. C.-H. Yeow, and P. Valdivia y Alvarado, "Freeform liquid 3D printing of soft functional components for soft robotics," ACS Appl. Mater. Interfaces **14**, 2301–2315 (2022).
[24]L. M. Friedrich, R. T. Gunther, and J. E. Seppala, "Suppression of filament defects in embedded 3D printing," ACS Appl. Mater. Interfaces **14**, 32561 (2022).
[25]T. Bhattacharjee, S. M. Zehnder, K. G. Rowe, S. Jain, R. M. Nixon, W. G. Sawyer, and T. E. Angelini, "Writing in the granular gel medium," Sci. Adv. **1**, e1500655 (2015).
[26]Y. Jin, A. Compaan, W. Chai, and Y. Huang, "Functional nanoclay suspension for printing-then-solidification of liquid materials," ACS Appl. Mater. Interfaces **9**, 20057–20066 (2017).
[27]T. J. Hinton, Q. Jallerat, R. N. Palchesko, J. H. Park, M. S. Grodzicki, H.-J. Shue, M. H. Ramadan, A. R. Hudson, and A. W. Feinberg, "Three-dimensional printing of complex biological structures by freeform reversible embedding of suspended hydrogels," Sci. Adv. **1**, e1500758 (2015).
[28]M. E. Cooke and D. H. Rosenzweig, "The rheology of direct and suspended extrusion bioprinting," APL Bioeng. **5**, 011502 (2021).
[29]M. Jalaal, G. Cottrell, N. Balmforth, and B. Stoeber, "On the rheology of Pluronic F127 aqueous solutions," J. Rheol. **61**, 139–146 (2017).
[30]G. P. Roberts and H. A. Barnes, "New measurements of the flow-curves for Carbopol dispersion without slip artefacts," Rheol. Acta **40**, 499–503 (2001).
[31]W. Feng, Y. Chai, J. Forth, P. D. Ashby, T. P. Russell, and B. A. Helms, "Harnessing liquid-in-liquid printing and micropatterned substrates to fabricate three-dimensional all-liquid fluidic devices," Nat. Commun. **10**, 1095 (2019).
[32]R. Xu, T. Liu, H. Sun, B. Wang, S. Shi, and T. P. Russell, "Interfacial assembly and jamming of polyelectrolyte surfactants: A simple route to print liquids in low-viscosity solution," ACS Appl. Mater. Interfaces **12**, 18116–18122 (2020).
[33]C. Poon, "Measuring the density and viscosity of culture media for optimized computational fluid dynamics analysis of in vitro devices," J. Mech. Behav. Biomed. Mater. **126**, 105024 (2022).
[34]*OpenFOAM v8* (The OpenFOAM Foundation, 2020).
[35]Certain commercial equipment, instruments, or materials are identified in this paper in order to specify the experimental procedure adequately. Such identification is not intended to imply recommendation or endorsement by the National Institute of Standards and Technology, nor is it intended to imply that the materials or equipment identified are necessarily the best available for the purpose.
[36]G. Van Rossum and F. L. Drake, *Python 3 Reference Manual* (CreateSpace, Scotts Valley, CA, 2009).
[37]L. M. Friedrich, R. T. Gunther, and J. E. Seppala (2022). "Python tools for OpenFOAM simulations of filament shapes in embedded 3D printing," NIST Public Data Repository, https://doi.org/10.18434/mds2-2602.
[38]J. Ahrens, B. Geveci, and C. Law, *ParaView: An End-User Tool for Large Data Visualization* (Elsevier, 2005).
[39]L. M. Friedrich, R. T. Gunther, and J. E. Seppala (2022), "OpenFOAM simulations of stress mitigation strategies in embedded 3D bioprinting," NIST Public Data Repository, https://doi.org/10.18434/mds2-2604.
[40]J. Kajtez, M. F. Wessler, M. Birtele, F. R. Khorasgani, D. R. Ottosson, A. Heiskanen, T. Kamperman, J. Leijten, A. Martínez-Serrano, N. B. Larsen, T. E. Angelini, M. Parmar, J. U. Lind, and J. Emnéus, "Embedded 3D printing in self-healing annealable composites for functional patterning of human neural constructs," Adv. Sci. **2022**, 2201392.
[41]S. M. Damián and N. Nigro, "An extended mixture model for the simultaneous treatment of small-scale and large-scale interfaces," Int. J. Numer. Methods Fluids **75**, 547–574 (2014).
[42]S. M. Damián, "An extended mixture model for the simultaneous treatment of small-scale and large-scale interfaces," Ph.D. thesis (Universidad Nacional del Litoral, 2013).
[43]S. S. Deshpande, L. Anumolu, and M. F. Trujillo, "Evaluating the performance of the two-phase flow solver interFoam," Comput. Sci. Dis. **5**, 014016 (2012).
[44]T. Holtzmann, *Mathematics, Numerics, Derivations, and OpenFOAM* (Holzmann CFD, 2019).
[45]R. Burdis and D. J. Kelly, "3D bioprinting hardware," in *Polymer-based Additive Manufacturing* (Springer, 2019), pp. 161–186.
[46]S. M. Hull, L. G. Brunel, and S. C. Heilshorn, "3D bioprinting of cell-laden hydrogels for improved biological functionality," Adv. Mater. **34**, 2103691 (2022).
[47]M. Nooranidoost, D. Izbassarov, S. Tasoglu, and M. Muradoglu, "A computational study of droplet-based bioprinting: Effects of viscoelasticity," Phys. Fluids **31**, 081901 (2019).
[48]L. Friedrich, R. Collino, T. Ray, and M. Begley, "Acoustic control of microstructures during direct ink writing of two-phase materials," Sens. Actuators, A **268**, 213–221 (2017).
[49]Y. Sriphutkiat, S. Kasetsirikul, D. Ketpun, and Y. Zhou, "Cell alignment and accumulation using acoustic nozzle for bioprinting," Sci. Rep. **9**, 17774 (2019).
[50]D. Leighton and A. Acrivos, "The shear-induced migration of particles in concentrated suspensions," J. Fluid Mech. **181**, 415–439 (1987).